Science of the Total Environment 643 (2018) 157–170

Contents lists available at ScienceDirect

Science of the Total Environment

journal homepage: www.elsevier.com/locate/scitotenv

Spatiotemporal distribution and national measurement of the global carbonate carbon sink

Huiwen Li [a,b,c], Shijie Wang [a,c], Xiaoyong Bai [a,c,*], Weijun Luo [a,c], Hong Tang [a], Yue Cao [a,b,c], Luhua Wu [a,b,c], Fei Chen [a,c,d], Qin Li [a,b,c], Cheng Zeng [a,c,d], Mingming Wang [a,b,c]

[a] State Key Laboratory of Environmental Geochemistry, Institute of Geochemistry, Chinese Academy of Sciences, 99 Lincheng West Road, Guiyang 550081, Guizhou Province, China
[b] University of Chinese Academy of Sciences, Beijing 100049, China
[c] Puding Karst Ecosystem Observation and Research Station, Chinese Academy of Sciences, Puding 562100, China
[d] School of Geography and Environmental Sciences, Guizhou Normal University, Guiyang 550081, China

HIGHLIGHTS

- Carbonate carbon sink is an important part of terrestrial sinks and missing sink.
- CCS amounts to nearly 75% of net forest sink have huge contribution to carbon budget.
- Tropical rainforest climate owns the greatest carbonate carbon sink flux.
- Global new production of multi-years' CCFS maps in a spatial resolution of 0.05°
- Separately carry out national measurement of 142 countries or regions for CCS

GRAPHICAL ABSTRACT

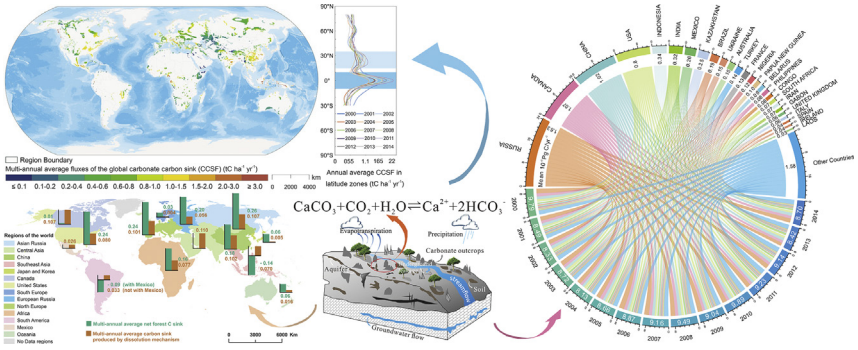

ARTICLE INFO

Article history:
Received 4 April 2018
Received in revised form 23 May 2018
Accepted 15 June 2018
Available online xxxx

Editor: R Ludwig

Keywords:
Carbonate carbon sink
National measurement
Missing sink
Carbon budget
Spatiotemporal evolution

ABSTRACT

The magnitudes, spatial distributions and contributions to global carbon budget of the global carbonate carbon sink (CCS) still remain uncertain, allowing the problem of national measurement of CCS remain unresolved which will directly influence the fairness of global carbon markets and emission trading. Here, based on high spatiotemporal resolution ecological, meteorological raster data and chemical field monitoring data, combining highly reliable machine learning algorithm with the thermodynamic dissolution equilibrium model, we estimated the new CCS of 0.89 ± 0.23 petagrams of carbon per year (Pg C yr^{-1}), amounting to 74.50% of global net forest sink and accounting for 28.75% of terrestrial sinks or 46.81% of the missing sink. Our measurement for 142 nations of CCS showed that Russia, Canada, China and the USA contribute over half of the global CCS. We also presented the first global fluxes maps of the CCS with spatial resolution of 0.05°, exhibiting two peaks in equatorial regions (10°S to 10°N) and low latitudes (10°N to 35°N) in Northern Hemisphere. By contrast, there are no peaks in Southern Hemisphere. The greatest average carbon sink flux (CCSF), i.e., 2.12 tC ha^{-1} yr^{-1}, for 2000 to 2014 was contributed by tropical rainforest climate near the equator, and the smallest average CCSF was presented in tropical arid zones, showing a magnitude of 0.26 tC ha^{-1} yr^{-1}. This research estimated the magnitudes, spatial distributions, variations and contributions to the global carbon budget of the CCS in a higher spatiotemporal representativeness and expandability way, which, via multiple mechanisms, introduced an important sink in the terrestrial carbon sink system and the global missing sink and that can help us further reveal and support our understanding of global rock weathering

* Corresponding author.
E-mail address: baixiaoyong@vip.skleg.cn (X. Bai).

https://doi.org/10.1016/j.scitotenv.2018.06.196

carbon sequestration, terrestrial carbon sink system and global carbon cycle dynamics which make our understanding of global change more comprehensive.

1. Introduction

Slight variations in the global or regional carbon cycles and budget can cause significant fluctuations of atmospheric CO_2 concentrations, which further affects the stability of the global climate (Raupach, 2011). Hence, controlling climate change by restricting global greenhouse gases requires a profound understanding of the mechanisms of the global carbon cycle, including its sources and sinks and their global spatiotemporal distributions and changes. However, the sources, magnitudes, variations, and locations of the terrestrial sinks (TCS) remain uncertain (Pan et al., 2011). To solve these problems, scientists have performed many studies. The Intergovernmental Panel on Climate Change (IPCC) estimated that the uptake by terrestrial ecosystems ranged from 1.9 to 2.3 ± 1.3 Pg C yr^{-1} from the 1980s to the 1990s (Watson et al., 2000). More studies have estimated a terrestrial C sink in the range of 0.3 to 4.8 Pg C yr^{-1} in these two periods (House et al., 2003; Melnikov and O'Neill, 2006). For the 2000s, studies (Landschutzer et al., 2014; Poulter et al., 2014) have shown that this sink was approximately 2.6 Pg C yr^{-1}. To determine the sources of the terrestrial sink, many scholars have made outstanding contributions, but previous studies have mainly focused on the forest carbon sink, agricultural soil erosion sink, etc. One study (Van Oost et al., 2007) showed that the agricultural soil erosion sinks range from 0.06 to 0.27 Pg C yr^{-1} and is not an important sink for the global carbon cycle. However, even if the net forest carbon sink is cut from the terrestrial sink system, the global carbon cycle is still unbalanced, leaving the familiar problem of the missing carbon sink (Schindler, 1999; Nilsson et al., 2003).

Traditional theories stated that the dissolution of carbonate cannot produce carbon sinks; however, increasing numbers of studies showed that the dissolution mechanism of carbonate rocks will produce carbon sinks in the short and long terms due to the global water cycle and biogenic functions such as the photosynthetic uptake of aquatic organisms (Pokrovsky et al., 2005; Liu et al., 2011; Martin, 2017; Shen et al., 2017). Based on this, many scholars thought that the CCS is an important component of the global carbon sink system (Yuan, 1997; Liu and Zhao, 2000; Martin et al., 2013) and may be the source of the missing sink (Liu and Dreybrodt, 2015). However, the magnitudes, spatiotemporal distributions and variations of the global total CCS and CCSF in carbonate zones still remain uncertain. Hence, fully understanding the sources of terrestrial carbon cycle ecosystems, the magnitudes and spatiotemporal distributions, variations and contributions to the global carbon budget of CCS and CCSF is of great significance for more reasonable and effective controls of global climate change which are this study's objectives.

Here, based on high spatiotemporal resolution ecological, meteorological raster data and chemical field monitoring data, combining highly reliable machine learning algorithm with the thermodynamic dissolution equilibrium model, we presented new estimates of the CCS and CCSF from 2000 through 2014 in the global carbonate rock outcrops. For a full understanding of the distribution and variation characteristics of the CCS, we subdivided the global carbonate rock outcrops into classification systems of continents, regions and countries, and based on this classification, we presented statistics and analyses of their CCS values. We advanced our analyses by reporting the spatial distributions, past trends and variation characteristics of the CCSF across regions, climate zones and latitudinal zones based on our estimated maps of the CCSF at a spatial resolution of 0.05°. In addition, to illustrate the correctness and importance of the CCS, we compared our estimates with other studies in the same field and with the net forest sink for further discussions of their contributions to the global carbon budget.

2. Material and methods

2.1. Material

With the purpose of calculating the long-term global CCS and CCSF in global carbonate rock outcrops more accurately, we utilized many global initial data including daily land surface maximal and minimal temperature (°C), daily total precipitation (mm/d), MODIS MOD16 global terrestrial evapotranspiration and field monitoring Ca^{2+} concentration date. In addition, we used global climate classification data and region boundaries to analyze the spatial distribution characteristics of CCS and CCSF.

Global climate classification data is basically based on the most frequently used updated KÖPPEN-GEIGER world map of climate classification (Rubel and Kottek, 2010) (http://koeppen-geiger.vu-wien.ac.at/) which is based on recent data sets from the Climatic Research Unit (CRU) of the University of East Anglia and the Global Precipitation Climatology Centre (GPCC) at the German Weather Service.

Carbonate rock outcrops are based on the v3.0 revision world map of carbonate rock outcrops from Geography and Environmental Science, University of Auckland (http://www.sges.auckland.ac.nz/sges_research/karst.shtm), which is in greater detail than the last two versions. In addition, the region boundaries are also from their database. The area of carbonate rock outcrops provides an upper limit on the area of exposed karst terrain. Extensive karstified carbonate rock also exists in sub crop, but is hard to map. Hence, here we only considered the carbonate rock outcrops.

The MODIS MOD16 global terrestrial evapotranspiration datasets (E) are gathered from Climate Office of Montana University (http://climate.umt.edu/products/evapotranspiration/), which are estimated using Mu et al.'s improved ET algorithm (Mu et al., 2011) based on the Penman-Monteith equation. The improved E estimates were testified to capture the magnitudes of the E measurements better than the previous version.

Global temperature data and global unified precipitation data are provided by the Climate Prediction Center (CPC) of National Oceanic and Atmospheric Administration (NOAA/OAR/ESRL PSD, Boulder, Colorado, USA) from their website (http://www.esrl.noaa.gov/psd/).

We utilized >20 years' chemical field monitoring data accumulated by many scientific workers in our team which can be obtained by contacting with the corresponding author. The Ca^{2+} concentration is monitored in karst observation station (Muzhudong point, Pudding Karst Observation Station, Guizhou, China) 3 to 4 times per month from January 1981 to December 2001 (Table 1).

2.2. Data processing methods

To estimate accurate CCS and CCSF, many methods were used. First, we assimilated all of the initial spatial data sets (precipitation (P), temperature (T), evapotranspiration (E)) to the same spatial-temporal scale (0.05°, monthly from 2000.1 to 2014.12) by a convolution model (Evensen, 2013). Then, we used the maximal information coefficient (MIC) (Reshef et al., 2011) to precisely quantify the correlations between the Ca^{2+} concentration and the P and T. Based on these quantitative relationships, the random forest method (RF) (Breiman, 2001) was utilized to establish the regression model of the Ca^{2+} concentrations and the P and T. Based on this regression model and the global P and T data sets, we calculated the global spatial ionic activity coefficient distribution maps of Ca^{2+}. After assimilating all the basic data, we used the

Table 1
Materials sources information.

Parameters	Time span	Temporal resolution	Sources
Precipitation (P)	2000.1–2014.12	Daily total	NOAA CPC
Temperature (T)	2000.1–2014.12	Daily	NOAA CPC
Evapotranspiration (E)	2000.1–2014.12	Monthly sum	Montana University
Ca^{2+} concentration	1981.1–2001.12	3 times per month	Monitoring station
Region boundaries	Present	/	University of Auckland
Carbonate rock outcrops	Present	/	University of Auckland
Climate classification	Present	/	University of Veterinary Medicine Vienna

thermodynamic dissolution equilibrium model for carbonate zones (Gaillardet et al., 1999; Zeng et al., 2016) to calculate the global carbon sinks produced by the dissolution mechanism (CCS) in the global carbonate zones.

2.3. The maximal information coefficient (MIC)

MIC belongs to a larger class of maximal information-based nonparametric exploration (MINE) statistics for identifying and classifying relationships. It can not only quickly identify interesting associations of data sets but also characterize them according to properties such as nonlinearity and monotonicity. MIC is based on the idea that if a relationship exists between two variables, then a grid can be drawn on the scatterplot of the two variables that partitions the data such that it encapsulates their relationship (Reshef et al., 2011). Then dynamic programming is used to achieve the largest possible mutual information in all the segmentation solutions. By normalizing and filtering, a final MIC of between 0 and 1 is derived. We used the MIC to precisely quantify the correlation between the Ca^{2+} concentrations and the P and T.

2.4. Random Forest regression (RF)

Combining bagging predictors and stochastic subspace identification (Breiman, 1996), Breiman proposed the random forest algorithm (RF) (Breiman, 2001). Using the resampling method of bootstrapping, RF creates tree structured classifiers via independent and identically distributed random vectors, i.e., RF randomly draws quantitative samples as training samples, deriving replacements from the original data set. Then, RF builds decision tree models for each training sample set. By voting for or calculating the average values of the predictions of multiple decision trees, the model derives the final classification or regression results. When the variables are numerical types, the model presents the final regression result by calculating the mean value of the predictions.

A large number of theoretical and practical studies have proved that the RF algorithm has high accuracy and stability, owning good tolerance for abnormal value and noise and hardly to over fit (Rodriguez-Galiano et al., 2014). The RF has gotten so many positive evaluations in machine learning, data mining and many fields (Verikas et al., 2011; Zhang et al., 2017). Also, Fernandez et al. evaluated 179 classifiers algorithms, the results showed that RF is the most outstanding one among these algorithms (Fernandez-Delgado et al., 2014).

Based on the quantitative relationships between the Ca^{2+} concentration and the P and T, we used the RF model and the global P and T raster data sets to calculate the distribution maps of the spatial ionic activity coefficient of Ca^{2+} in the global carbonate zones at a spatial resolution of 0.05°. In this study, we built the pixel based RF regression model according to the following steps.

First of all, we created the tree structure regression classifier, with the form of $\{h(X, \Theta_t), t = 1, \ldots, p\}$, consisted of independent and identically distributed random vector (Θ_t). Then, by quantificationally and randomly sampling with replacement from the training data set consisted of Ca^{2+} concentration in aquifer, P and T, we built a certain amount of independent decision trees. The randomly sampled training data set (X_i, Y_i) is mutually independent. Finally, by calculating the average value of all trees' calculation results of data set that needed for prediction, we got the final prediction of Ca^{2+} concentration in each pixel. For data set of X that needed for prediction, we used the following equation to calculate the corresponding Ca^{2+} concentration (Y_k):

$$Y_k = \arg ave\left(\sum_i^N h_i(x_k|(f_i))\right) \quad (1)$$

where Y_k is the prediction result of the kth sample set, arg ave($\cdot$) is averaging algorithm, $h_i(\cdot)$ is the calculation result of the ith regression tree, $x_k|(\cdot)$ is the kth input sample set.

Then, the accuracy of the model's prediction result is described by the mean square value of generalization error of the vector h(X) that need to be forecasted, which is calculated by Eq. (2):

$$E_{X,Y}(Y-h(X))^2 \quad (2)$$

where Y is the actual Ca^{2+} concentration of the training set X, h (X) is the predicted concentration of X. $E_{X,Y}(\cdot)^2$ represents the following equation:

$$E_{X,Y}(\cdot)^2 = \frac{1}{n}\sum_{t=1}^{n}(\cdot)^2 \quad (3)$$

In detail, the accuracy of the model was calculated by the mean squared error of data (out of bag, OOB) that didn't participate in the model training (MSE_{OOB}):

$$MSE_{OOB} = n^{-1}\sum_{i=1}^{n}\left(y_i-\hat{y}_i^{OOB}\right)^2 \quad (4)$$

where y_i is the ith actual Ca^{2+} concentration of OOB, $\hat{y}_i^{OOB}$ is the predicted value.

Besides, the model used another parameter which is called the percentage of explained variance (PVE) to evaluate the generalization ability of the model, which is calculated by the following equation:

$$R_{rf}{}^2 = 1-\frac{MSE_{OOB}}{\hat{\delta}_y{}^2} \quad (5)$$

where $\hat{\delta}_y{}^2$ is the total variance of the predicted result for OOB.

2.5. The thermodynamic dissolution equilibrium model for carbonate zones

Based on the usual equations for the dissolution of calcite at equilibrium given in (6), Gombert created the thermodynamic dissolution equilibrium model of Eq. (7) for carbonate zones with the assumption

Table 2
Coefficients of the formulas for the K_i factors and T_k.

	A	B	C	D	F
K_s	−171.9065	−0.077993	2839.3191	71.595	
K_1	−356.3094	−0.06091964	21,834.37	126.8339	−1,684,915
K_2	−107.8871	−0.03252849	5151.79	38.92561	−563,713.9

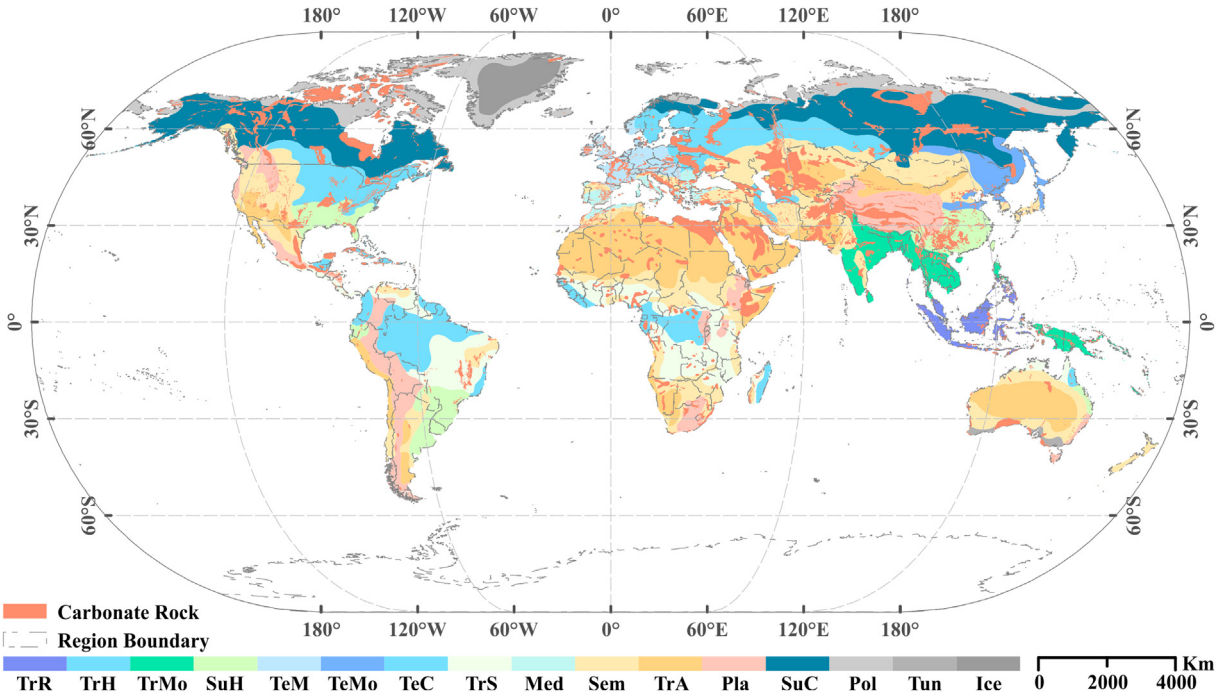

Fig. 1. Region boundaries, carbonate rock outcrops and climate classification. The abbreviations represent Tropical Rainforest, Tropical Humid, Tropical Monsoon, Subtropical Humid, Temperate Maritime, Temperate Monsoon, Temperate Continental, Tropical Savanna, Mediterranean, Semiarid, Tropical Arid, Plateau, Subarctic Continental, Polar, Tundra, Ice Sheets respectively. The carbonate outcrops presented here are all assumed to be calcite.

that the chemical reactions were at equilibrium in the local hydrological, meteorological and geochemical conditions (Gaillardet et al., 1999; Zeng et al., 2016).

$$CaCO_3 + CO_2 + H_2O \rightleftharpoons Ca^{2+} + 2HCO_3^- \quad (6)$$

$$D_{max} = 10^6 (P-E)\left[Ca^{2+}\right]_{eq} = 10^6 (P-E)\left(K_s K_1 K_0 / 4K_2 \gamma_{(Ca^{2+})}{}^3\right)^{1/3} (pCO_2)^{1/3} \quad (7)$$

In Eq. (7), D_{max} is the dissolution flux of calcite (mol km^{-2} yr^{-1}). Traditionally, due to the lack of high spatial-temporal resolution basic data (P, T, E, etc.) and high computational complexities, we usually use the cumulative data of the whole year from the limited field stations, which will lead to the poor spatiotemporal representativeness and expandability of the estimates. After solving this problem by using high spatial-temporal resolution basic data (monthly data at a spatial resolution of 0.05°) and better analysis and processing technologies (with python programming and GIS platforms), we derived the cumulative annual average D_{max} by calculating the monthly D_{max} from January 2000 to December 2014. Therefore, the basic data sets below are all given at a monthly scale. P and E are the monthly total precipitation and evapotranspiration (mm m^{-1}). K_s represents the calcite solubility constant with K_1 being the equilibrium constant of the CO_2 hydration and dissociation with the formation of bicarbonate ions. K_0 is the equilibrium constant of the CO_2 dissolution in water with K_2 representing the equilibrium constant of carbonate ion formation. $\gamma(Ca^{2+})$ is the activity coefficient of Ca^{2+} in solution. pCO_2 represents the partial pressure of CO_2 inside the aquifer (atm). For similar reasons, previous studies usually use constant K_i (i = s, 1, 2, 0) values at normal atmospheric temperature (15 °C), which will lead to some biases. The K_i

Table 3
Global annual average and multi-annual average carbon sink fluxes of the carbonate carbon sink (CCSF) (tC ha^{-1} yr^{-1}) in different climate types from 2000 to 2014.

Climate types	Annual average CCSF and multi-annual average CCSF (tC ha^{-1} yr^{-1}) in different climate types															
	2000	2001	2002	2003	2004	2005	2006	2007	2008	2009	2010	2011	2012	2013	2014	Mean
Tropical rainforest	2.29	1.85	1.30	1.90	1.53	1.95	1.95	2.17	2.92	1.78	2.81	2.50	2.18	2.54	1.95	2.11
Tropical monsoon	1.57	1.60	1.15	1.41	1.08	1.71	1.32	1.55	1.68	1.40	1.76	1.88	1.79	2.00	1.41	1.55
Subtropical humid	1.20	1.09	1.32	0.98	1.08	0.97	0.98	1.06	1.29	1.01	1.18	0.95	1.10	1.10	1.23	1.10
Tropical savanna	1.53	1.02	1.11	1.03	1.08	1.06	1.20	1.12	0.99	0.93	1.10	1.04	0.88	0.96	0.77	1.05
Tropical humid	1.14	0.87	0.87	0.83	0.76	0.90	0.86	1.17	0.92	0.83	1.20	1.31	1.23	1.05	1.22	1.01
Temperate maritime	1.07	0.76	0.99	0.57	0.62	0.69	0.85	0.86	0.93	0.96	0.96	0.84	1.09	0.66	0.92	0.85
Temperate continental	0.88	0.77	0.73	0.87	0.80	0.69	0.82	0.74	0.88	0.98	0.88	0.78	0.80	0.64	0.70	0.80
Temperate monsoon	0.83	0.62	0.70	0.79	0.69	0.70	0.75	0.81	0.69	0.95	0.98	0.88	0.85	0.78	0.75	0.79
Plateau	0.67	0.69	0.62	0.73	0.67	0.68	0.61	0.68	0.76	0.65	0.76	0.74	0.72	0.71	0.77	0.70
Mediterranean	0.69	0.74	0.78	0.72	0.60	0.76	0.51	0.62	0.58	0.83	0.86	0.54	0.84	0.50	0.87	0.70
Subarctic continental	0.68	0.62	0.57	0.61	0.56	0.71	0.75	0.75	0.73	0.66	0.67	0.65	0.62	0.55	0.68	0.65
Polar	0.66	0.54	0.44	0.69	0.52	0.64	0.65	0.70	0.61	0.68	0.70	0.57	0.58	0.45	0.53	0.60
Semiarid	0.60	0.52	0.50	0.54	0.54	0.52	0.55	0.54	0.53	0.54	0.62	0.60	0.56	0.54	0.55	0.55
Tundra	0.63	0.44	0.27	0.44	0.40	0.38	0.16	0.37	0.41	0.43	0.38	0.45	0.36	0.59	0.33	0.40
Tropical arid	0.26	0.19	0.24	0.30	0.25	0.21	0.32	0.27	0.26	0.27	0.29	0.33	0.26	0.26	0.21	0.26

The above climate types are modified by the updated KÖPPEN-GEIGER world map of climate classification (Rubel and Kottek, 2010). The Ice Sheets climate has no carbonate zones distribution so there's no CCSF in this climate. According to the above CCSF in global climate types, we calculated the multi-annual CCSF of global carbonate outcrops from 2000 to 2014 with the magnitude of 0.87 tC ha^{-1} yr^{-1}.

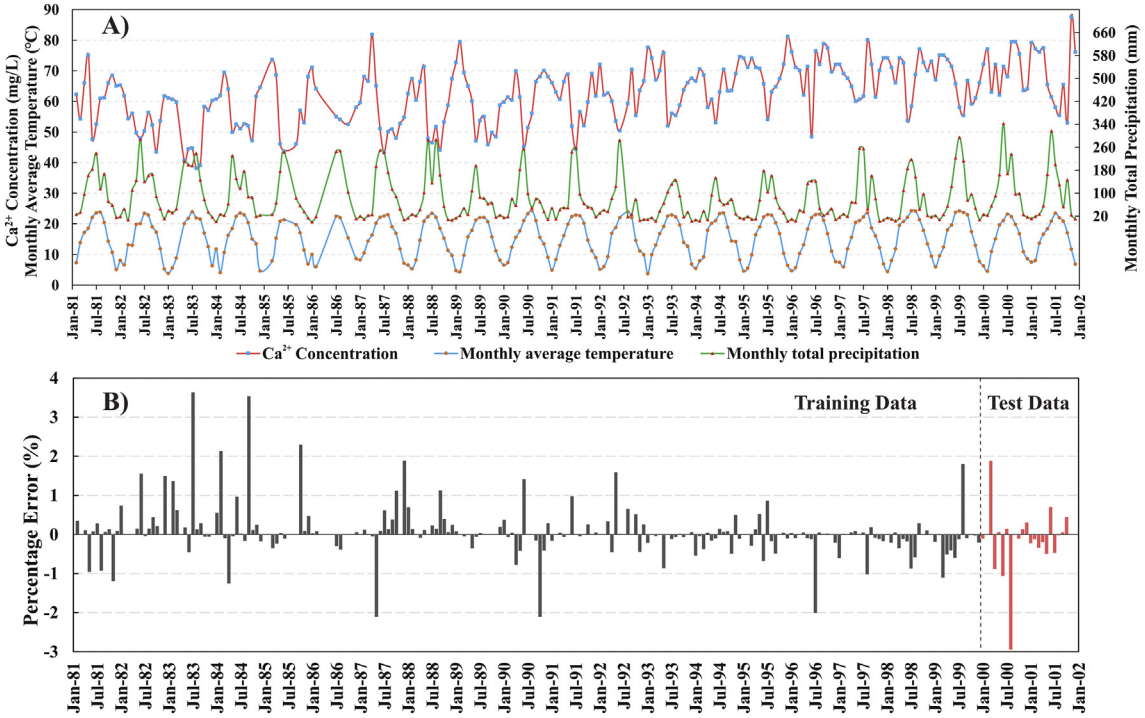

Fig. 2. Distribution relationships of Ca^{2+} concentration in aquifer with T, P and percentage errors of fitted Ca^{2+} concentration by RF model. (A) shows the distribution relationships among Ca^{2+} concentration, monthly average temperature and monthly total precipitation from January 1981 to December 2001 and (B) represents the percentage errors of fitted Ca^{2+} concentration by RF model with parameters of monthly average temperature and monthly total precipitation from Jan 1981 to Dec 2001.

factors are extremely sensitive to temperature changes (Plummer and Busenberg, 1982) and are functions of temperature (T_k in the Kelvin temperature scale) (Table 2).

$$log(K_s) = A + BT_k + C/T_k + Dlog(T_k) \tag{8}$$

$$log(K_1) = A + BT_k + C/T_k + Dlog(T_k) + F/{T_k}^2 \tag{9}$$

$$log(K_2) = A + BT_k + C/T_k + Dlog(T_k) + F/{T_k}^2 \tag{10}$$

$$K_0 = 1.7 \times 10^{-4}/K_1 \tag{11}$$

The ionic activity coefficients of Ca^{2+} are calculated by the Debye-Hückel equation (Plummer and Busenberg, 1982).

$$log(\gamma_i) = -AZ_i{}^2\frac{\sqrt{I}}{1 + Ba_i\sqrt{I}} \tag{12}$$

where Z_i is the ionic electric charge of Ca^{2+}, a_i represents the ionic radius of Ca^{2+}, which is 6 Å (Dreybrodt, 1988). A and B are determined by temperature (T in Celsius temperature scale) as shown in formula (13) and (14) respectively, and I is the ionic strength described in formula (15).

$$A = 0.4883 + 8.074 \times 10^{-4}T \tag{13}$$

$$B = 0.3241 + 1.6 \times 10^{-4}T \tag{14}$$

$$I = \frac{1}{2}\sum_i Z_i{}^2C_i \tag{15}$$

where C_i is the ionic concentration (mol L^{-1}). pCO_2 is calculated from Brook's formula (Brook et al., 1983) as follows.

$$log(pCO_2) = -3.47 + 2.09 \times \left(1 - e^{-0.00172E}\right) \tag{16}$$

Theoretically, the dissolution of each mole of $CaCO_3$ consumes one mole CO_2. Thus, in carbonate rock outcrops, the CCSF can be calculated by the following equation:

$$\begin{aligned} CCSF &= 10^6(P-E)[HCO_3{}^-]_{eq}/2 = 10^6(P-E)\left[Ca^{2+}\right]_{eq} \\ &= 10^6(P-E)\left(K_sK_1K_0/4K_2\gamma_{(Ca^{2+})}{}^3\right)^{1/3}(pCO_2)^{1/3} \end{aligned} \tag{17}$$

2.6. The uncertainty of the estimates

Many climatic, hydrological, meteorological and field monitoring datasets were used in the study; hence, in order to improve the reliability of the results as much as possible, we optimized both the selection of the basic data and utilization of methods. For long-term field monitoring data from January 1981 to December 2001, we first selected observation stations far away from human habitations and adopted a sampling scheme that monitoring the Ca^{2+} concentration 3 to 4 times per month. Then, we calculated the monthly average values of these monitoring data. For the basic data, we chose the high spatiotemporal daily total precipitation raster, the daily maximal and minimal temperature raster (these three types of raster data are provided by the Global Telecommunications System (GTS) from the long-term monitoring data gathered by >16,000 gauge stations (Chen et al., 2008) globally rather than via satellite observation data with high uncertainties caused by cloud and mist) and the terrestrial evapotranspiration calculated by the improvement algorithm (Mu et al., 2011). Based on these basic data, we present the global spatial maps of the monthly precipitation, monthly average temperature and monthly evapotranspiration from January 2000 to December 2014. In addition, the RF algorithm we used for the global spatial maps of the ionic activity coefficient of Ca^{2+} is proven to be highly reliable and robust (Guo et al., 2004). According to all these approaches, we used global high-spatial-resolution hydrological and meteorological data (raster data, not point data) and long-term field monitoring data based on a thermodynamic dissolution

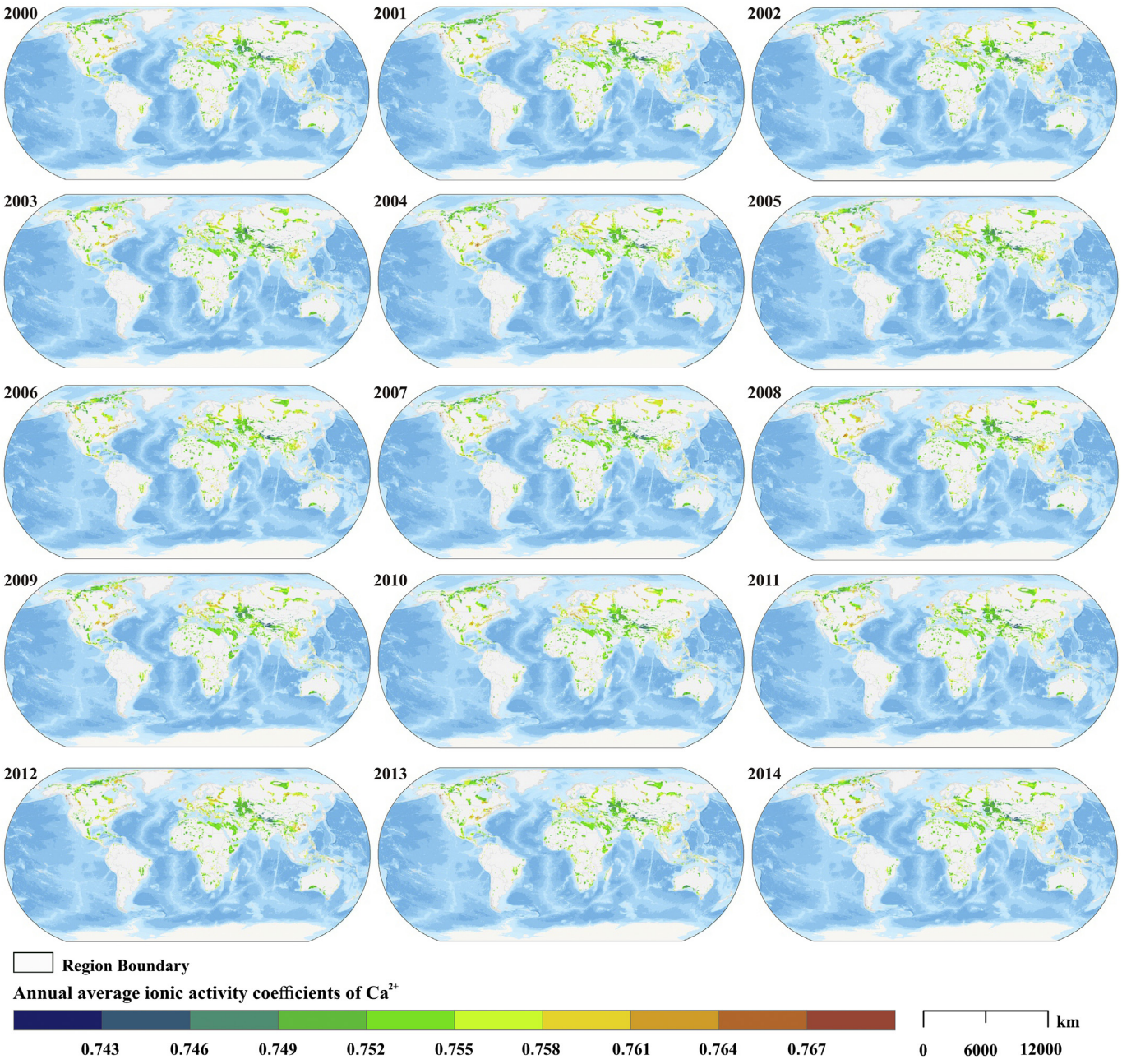

Fig. 3. Annual average ionic activity coefficients of Ca^{2+} in aquifer of carbonate rock outcrops from 2000 to 2014.

equilibrium model that fully considers the actual hydrological and hydrochemical conditions of specific carbonate regions and separately calculates the CCS of each pixel at a resolution of 0.05°. All of these schemes can make our estimates have relatively high reliabilities.

Specifically, the uncertainties of our estimates include two parts which are the uncertainties of the data and models. First, to resolve the uncertainties of the data, three models were used to measure the uncertainties of the global precipitation and surface temperature data by Chen (Chen et al., 2008). The results show that all three objective techniques are capable of generating useful daily precipitation analyses with biases that are generally <1% over most parts of the global land areas. Hence, we defined the uncertainties of the precipitation and temperature as 1%. For evapotranspiration, six new approaches were used to improve the data, and the average of the two mean absolute biases (MAE) of the improved algorithm is 24.35% (Mu et al., 2011). Therefore, the uncertainty of the evapotranspiration is defined as 24.35%. We defined the uncertainty of the monitoring Ca^{2+} concentration as 5% for its confidence interval of 95%. Then, for the uncertainties of the models,

Fig. 4. Global annual fluxes of the global carbonate carbon sink (CCSF) and the distribution of multiannual average in global carbonate zones from 2000 to 2014. The above figures show the spatial distribution of CCSF of each year. The high values of CCSF are mainly located in the equatorial regions where the temperature and rainfall are relatively abundant that can promote the process of dissolution. In contrast, the low values are mainly located in pleases where has poor hydrological conditions such as plateau and desert zones in Central Asia and Northern Africa, cold zones in the Northern Hemisphere and so on. A) is the distribution map of the multiannual average carbon sink fluxes produced by the dissolution mechanisms from 2000 to 2014 at a spatial resolution of 0.05°, the scale is for A) only. B) are curve distributions of the annual average CCSF in the latitudinal zones (80°N-30°S) of each year. The regions beyond 80°N and 30°S have barely any carbonate zones; hence, at these latitude zones, there are no CCSF. The regions marked in blue in B) (10°S-10°N, 15°N-35°N) are the two peaks of the CCSF in the equatorial regions and low latitudes of the Northern Hemisphere. (For interpretation of the references to colour in this figure legend, the reader is referred to the web version of this article.)

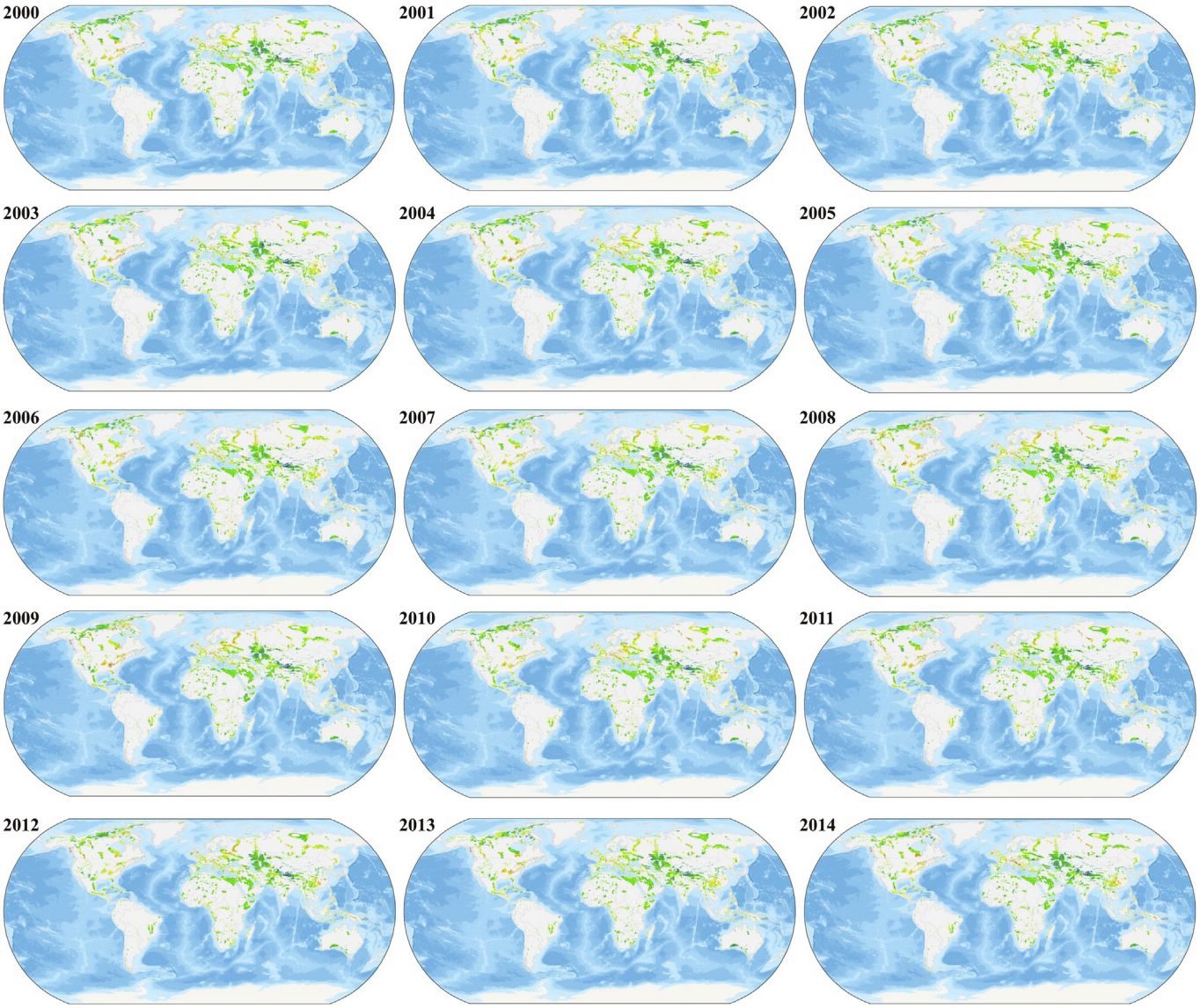
2000
2001
2002
2003
2004
2005
2006
2007
2008
2009
2010
2011
2012
2013
2014

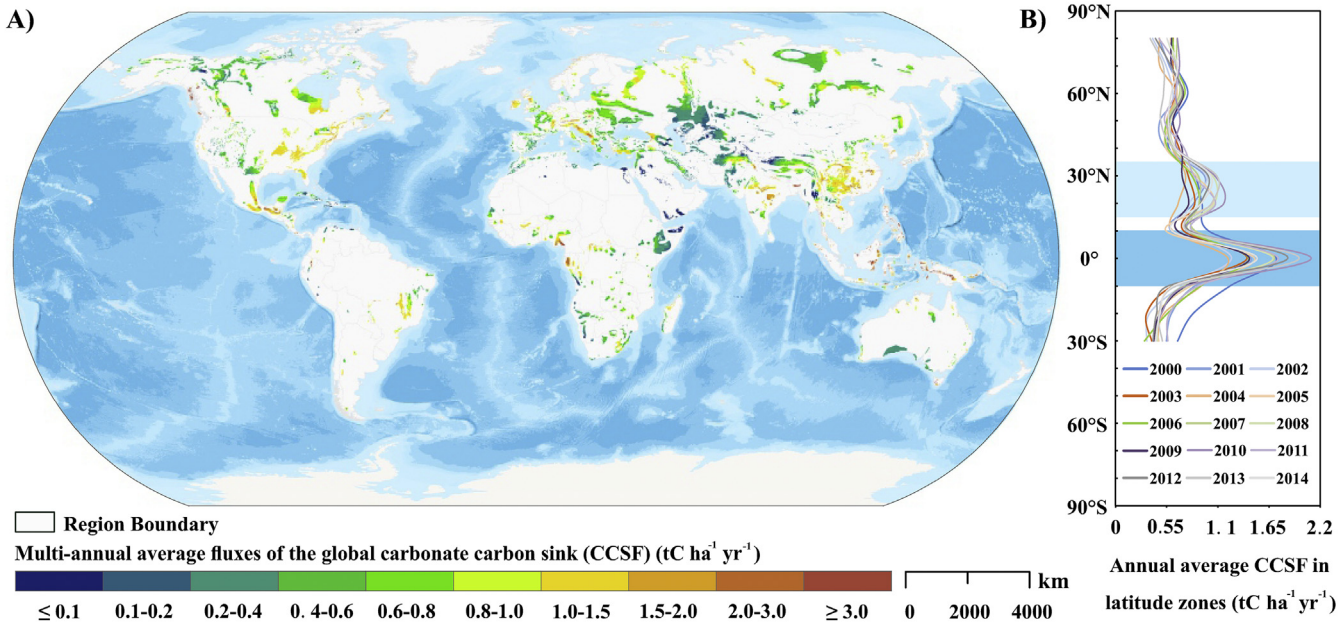
A)
B)
90°N
60°N
30°N
0°
30°S
60°S
90°S
2000 2001 2002
2003 2004 2005
2006 2007 2008
2009 2010 2011
2012 2013 2014
0 0.55 1. 1 1.65 2.2
Annual average CCSF in latitude zones (tC ha-1 yr-1)
Region Boundary
Multi-annual average fluxes of the global carbonate carbon sink (CCSF) (tC ha-1 yr-1)
≤ 0.1 0.1-0.2 0.2-0.4 0. 4-0.6 0.6-0.8 0.8-1.0 1.0-1.5 1.5-2.0 2.0-3.0 ≥ 3.0
0 2000 4000 km

the RF regression model based on the long-term monitoring Ca^{2+} concentration presents a percentage error of less than ±4% between the fitting results and the monitoring data; hence, we defined the uncertainty of the fitting concentration of Ca^{2+} as 4%. Based on the uncertainty model (Landschutzer et al., 2014), we derived the final uncertainty of our estimates to be 25.93%.

$$\sigma = \sqrt{\sum_{i=1}^{n} \sigma_i^2} \tag{18}$$

The uncertainty of data in this study is present in the form of y ± x. Note that the uncertainty cannot completely reflect the accuracy of our estimates as this uncertainty is the accumulation of the maximum uncertainties of all the data and models, hence, represents the maximum bias of our estimates. The specific bias or uncertainty of each pixel of the estimated spatial maps is different and should be determined by the actual hydrological, meteorological and field monitoring data in that pixel.

3. Results

3.1. Ionic activity coefficients of Ca^{2+} in aquifer of carbonate rock outcrops

According to the measured Ca^{2+} concentration in aquifer monitored in karst observation station from January 1981 to December 2001, we got the following concentration distributing phenomenon (Fig. 2). The T and P share the synchronous variation trend, i.e., when T grows up, P gets stronger almost at the same time, and when T cools down, P becomes negative. That's because T affects E, more water will gather into the clouds due to the increases in E. Hence, more water in clouds, more P will reach to the surface. In carbonate rock outcrops, a clear dominance of the Ca^{2+} concentration is apparent for all cold periods (around November to March), and in warm periods (around July), it shows the opposite situation, i.e., the Ca^{2+} concentration is in the negative level among the periods. The Ca^{2+} concentration variations in the long term shown above can be readily explained by the oscillation of the T and P. Peaks in Ca^{2+} concentration around January result from the decreases of T and P. The decreasing T makes the partial pressure of CO_2 in aquifer stronger than that in warm situation which promotes the equilibrium reaction go to the positive process, at the same time, P reaches to its perfect negative level which makes it hard to recharge soil moisture and dilute the solution, hence, the Ca^{2+} concentration reaches to the maximum in this period. Conversely, high T and P account for the minimum of Ca^{2+} concentration in the period.

We used MIC to quantify the correlation between Ca^{2+} concentration and P, T. The result shows that the correlation between Ca^{2+} concentration and P, T are 0.37 and 0.3 respectively, which means Ca^{2+} concentration can be fitted by P and T. To obtain more accurate Ca^{2+} concentration by P and T, based on the measured Ca^{2+} concentration dataset and corresponding P, T in the same period, we established the Random Forest model. Data from Jan 1981 to Dec 1999 were used to build the fitting model, these data and the rest data (Jan 2000 to Dec 2001) were all utilized to test the model. After generating 500 regression trees, the model reached its steady state with mean of squared residuals of 0.39 and percent variance explained of 99% which reflect the high reliability and robustness of the model. The gray bars are training

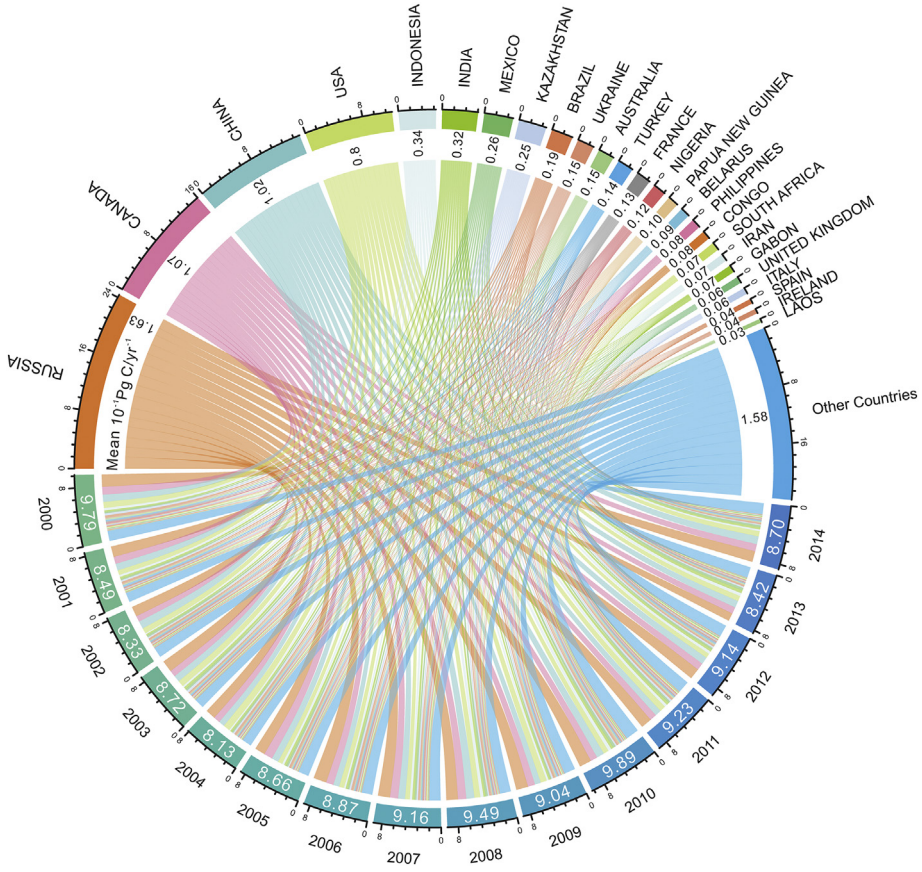

Fig. 5. CCS of countries from 2000 to 2014 (all in 10^{-1} Pg C yr^{-1}). The arcs in upper graph represent the total CCS of each country in the 15 years from 2000 to 2014. The values below each country show the multiannual average CCS of this country. Each country has 15 histograms from the upper semicircle to the bottom, and each histogram represents the total CCS of each year, expressing the magnitude with width. The bottom semicircle is divided into 15 bar charts, which represent each year's total CCS within the global carbonate zones. Each bar chart is the sum of every countries' CCS in the corresponding year. The graph shows the distributions and variations of the 26 countries' CCS. Other countries' CCS are too small to show if they are separated; thus, we calculated the sum CCS, which accounts for approximately 11.78% of the global CCS.

data from Jan 1981 to Dec 1999 that participated in the RF model establishing and the red bars are test data from Jan 2000 to Dec 2001. The percentage errors of all data are in the range of ±4%.

According to our RF regression model and global monthly total precipitation and monthly average temperature data, we estimated the global annual ionic activity coefficients of Ca^{2+} in aquifer of each month from January 2000 to December 2014 and then we calculated the average value of 12 months for each year, i.e. the annual ionic activity coefficients of Ca^{2+}. The coefficients reflect the extent of the chemical reaction. Globally, the high coefficients are located in equatorial regions and middle and low latitude regions in the Northern Hemisphere (southwest of China, Alps in central and southern Europe, the European Mediterranean areas, Ural Mountains and east-central America). The coefficients are range from 0.743 to 0.767 in the study period in a steady state shown as Fig. 3.

3.2. Distribution and variation of the CCSF

The multiannual average CCSF in the global carbonate zones from 2000 to 2014 was estimated to be 0.87 tons of carbon per hectare per year (tC km^{-2} yr^{-1}). The spatial distribution characteristics are highly dependent on the regional climatic and hydrological conditions (Bai and Dent, 2009; Y. Li et al., 2016; Zeng et al., 2017). Hence, high values of CCSF are mainly located in the equatorial regions where the temperatures and rainfalls are relatively abundant and can promote the process of dissolution. In contrast, the low values are mainly located in those zones with poor hydrological conditions, such as the plateau and desert zones in Central Asia and Northern Africa and the cold zones in the Northern Hemisphere. This phenomenon can be easily observed via the global statistics of the different latitude zones concerning the CCSF (Fig. 4 B). A clear dominance of the CCSF change signals (1.25–-2.17 tC ha^{-1} yr^{-1}) in the equatorial regions (10°S to 10°N) is apparent for all years. There is another peak in the low latitudes (10°N to 35°N) of the Northern Hemisphere, and the carbonate zones in southwestern China are the main contributors to this pattern (Wang et al., 2004; Tian et al., 2016). In the high-latitude regions of the Northern Hemisphere, the CCSF show a decreasing trend with increasing latitude, with slight fluctuations in some regions due to the uneven spatial distributions of the CCSF. CCSF in the Southern Hemisphere are much lower than those in the Northern Hemisphere at the same latitudes; moreover, there are no peaks in the Southern Hemisphere between 10°S and 30°S, as there are barely any carbonate zones in the high latitude regions (beyond 30°S) of the Southern Hemisphere. Only the middle and low latitude regions (0°S to 30°S) produce carbonate carbon sink. The reasons for the different distributions of the CCSF at different latitude zones lie in the climatic and hydrological conditions of the different latitudes.

Global climate change is closely related to regional climate (B.G. Li et al., 2016a). Hence, in order to explore the relationship between the CCSF and the climate, we extend our analyses by calculating the average CCSF values in each climate classification (Fig. 1) of the study period (Table 3). The greatest average carbon sink flux, i.e., 2.11 tC ha^{-1} yr^{-1}, for 2000 to 2014 was contributed by the tropical rainforest climate near the equator, and the smallest average CCSF values were present in the tropical arid zones, showing a magnitude of 0.26 tC ha^{-1} yr^{-1}. In tropical climate regions, the CCSF of the tropical rain forest and tropical monsoon climate zones showed an increasing and then decreasing trend. In contrast, the CCSF in the tropical and subtropical humid climate zones presented a decreasing and then increasing trend. In addition, the tropical arid zones presented an intense fluctuation of the CCSF. Notably, tropical savanna zones showed a continually decreasing trend of CCSF during this period. In the temperate climate zones, the CCSF of the temperate continental and monsoonal climate zones demonstrated increasing and then decreasing trends. However, the

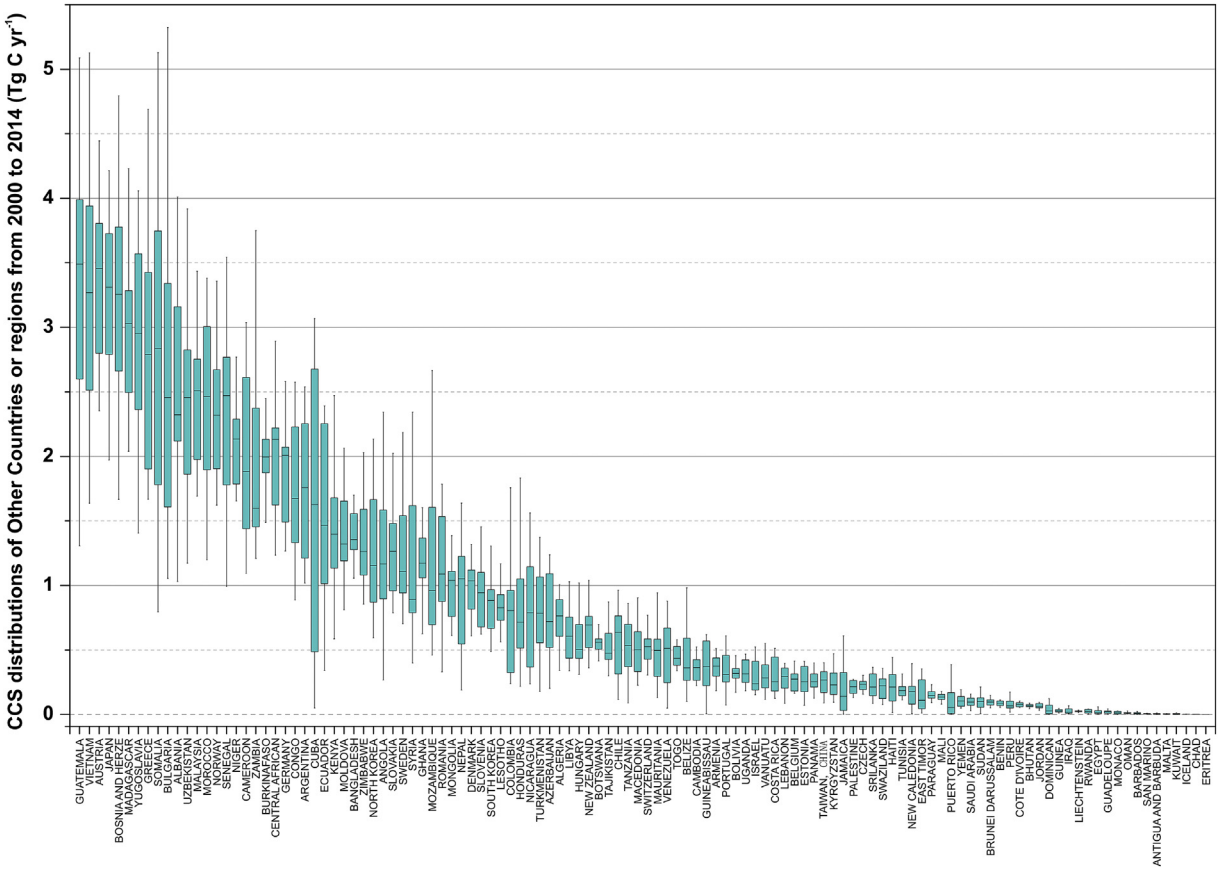

Fig. 6. CCS distributions of other 116 countries or regions from 2000 to 2014 (Tg = 10^{12} g C).

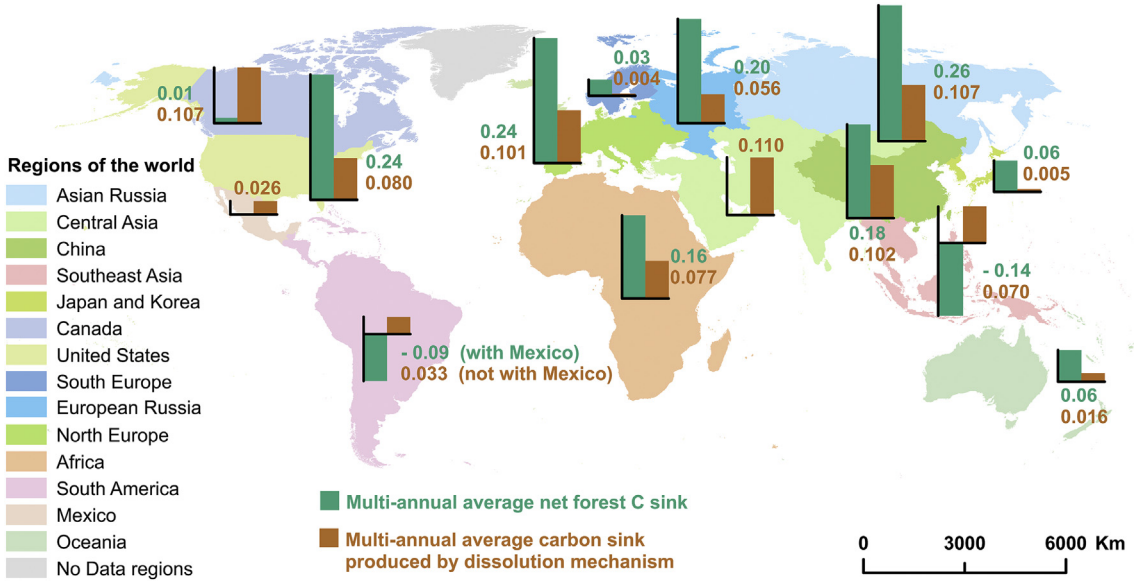

Fig. 7. Spatial distribution map of multiannual average carbon sinks produced by the dissolution mechanisms from 2000 to 2014 of regions and the corresponding net forest carbon sinks. The classification scheme is set according to Pan's research and is also the source of the net forest C sink data (see Pan et al. (2011) for more details). The coloured bars in the down-facing direction represent the negative sinks or carbon emissions. The net forest sinks are missing in Central Asia, and the net forest sink of South America includes Mexico (Pan et al., 2011). However, when we calculate the CCS, due to the large magnitude of the Mexico in CCS, we separated Mexico from South America. (For interpretation of the references to colour in this figure legend, the reader is referred to the web version of this article.)

temperate maritime zones showed decreasing and then increasing trends. In arid and cold climate zones, plateau climate zones showed relatively stable variations of CCSF from 2000 to 2014 with an increase of 14.7%. In contrast, the CCSF in the Mediterranean climate zones showed intense fluctuations over the study period, especially from 2008 to 2014, with increments of up to 74% (from 0.50 ha^{-1} in 2013 to 0.87 tC ha^{-1} in 2014). Similarly, the subarctic continental, polar and tundra zones all presented intense CCSF fluctuations; however, the CCSF in the semiarid zones showed relatively stable characteristics.

3.3. Spatiotemporal characteristics and national measurement of the CCS

The CCS of the global carbonate zones was estimated to be 0.894 ± 0.232 Pg C yr^{-1} from 2000 to 2014. Different regions had special variation characteristics geographically (Table 4). Asia, owing to its huge carbonate rock distribution area of 5.738×10^6 km^2, had the world's largest CCS, reaching 0.394 ± 0.102 Pg C yr^{-1} in this period (44.07% of the global CCS). North America contributed a CCS of 0.220 ± 0.057 Pg C yr^{-1} (24.7% of the global CCS) during the study period. Europe's CCS (0.160 ±

Table 4
Annual total and multi-annual average carbonate carbon sink (CCS) (Pg C yr^{-1}) in continents and regions' carbonate rock outcrops from 2000 to 2014 and corresponding carbonate rock outcrops area (C area) ($\times 10^6$ km^2).

Regions	C area (10^6 km^2)	Annual total CCS and multi-annual average CCS (Pg C yr^{-1}) in continents and regions' carbonate rock outcrops															
		2000	2001	2002	2003	2004	2005	2006	2007	2008	2009	2010	2011	2012	2013	2014	Mean
Asia	5.738	0.400	0.377	0.347	0.392	0.326	0.382	0.394	0.419	0.421	0.385	0.448	0.426	0.412	0.390	0.389	0.394
Central Asia	2.448	0.094	0.104	0.087	0.127	0.095	0.100	0.116	0.119	0.094	0.114	0.119	0.135	0.124	0.115	0.100	0.110
Asian Russia	1.700	0.116	0.097	0.094	0.106	0.090	0.107	0.129	0.123	0.114	0.115	0.121	0.106	0.096	0.081	0.110	0.107
China	1.166	0.106	0.101	0.114	0.095	0.088	0.101	0.089	0.103	0.120	0.088	0.113	0.092	0.106	0.101	0.116	0.102
Southeast Asia	0.395	0.079	0.070	0.048	0.058	0.047	0.069	0.054	0.068	0.088	0.063	0.089	0.086	0.079	0.088	0.058	0.070
Japan & Korea	0.029	0.005	0.005	0.004	0.006	0.005	0.005	0.006	0.006	0.005	0.005	0.007	0.007	0.007	0.005	0.005	0.005
North America	2.418	0.205	0.173	0.169	0.187	0.193	0.194	0.184	0.187	0.208	0.198	0.182	0.190	0.172	0.177	0.184	0.187
Canada	1.555	0.116	0.103	0.088	0.096	0.095	0.128	0.111	0.119	0.122	0.106	0.104	0.101	0.105	0.098	0.108	0.107
USA	0.863	0.089	0.070	0.081	0.091	0.098	0.066	0.073	0.068	0.086	0.092	0.078	0.089	0.067	0.079	0.076	0.080
Europe	2.156	0.181	0.158	0.167	0.153	0.151	0.150	0.159	0.155	0.164	0.185	0.189	0.139	0.186	0.114	0.156	0.161
South Europe	1.343	0.110	0.094	0.110	0.085	0.091	0.102	0.092	0.099	0.106	0.121	0.130	0.081	0.118	0.074	0.107	0.101
European Russia	0.784	0.066	0.060	0.054	0.064	0.057	0.044	0.063	0.053	0.055	0.061	0.056	0.054	0.064	0.037	0.046	0.056
North Europe	0.029	0.005	0.004	0.003	0.004	0.003	0.004	0.004	0.003	0.003	0.003	0.003	0.004	0.004	0.003	0.003	0.004
Africa	1.279	0.104	0.071	0.079	0.070	0.070	0.059	0.084	0.089	0.067	0.073	0.080	0.080	0.082	0.077	0.074	0.077
America	0.616	0.064	0.055	0.061	0.055	0.057	0.065	0.057	0.051	0.071	0.049	0.072	0.064	0.048	0.068	0.055	0.059
South America	0.383	0.043	0.033	0.033	0.027	0.035	0.039	0.035	0.026	0.039	0.030	0.036	0.037	0.026	0.032	0.026	0.033
Mexico	0.233	0.021	0.022	0.028	0.028	0.022	0.026	0.022	0.025	0.032	0.019	0.036	0.027	0.022	0.036	0.029	0.026
Oceania	0.270	0.025	0.016	0.011	0.014	0.015	0.015	0.010	0.015	0.016	0.015	0.017	0.023	0.014	0.016	0.014	0.016
Global	12.476	0.979	0.849	0.833	0.872	0.813	0.866	0.887	0.916	0.949	0.904	0.989	0.923	0.914	0.842	0.870	0.894

The classification scheme is according to Pan's research (Pan et al., 2011). The basic data (P, T, E) are missing in plateaus in Central Asia, some arid regions in the Middle East, deserts in northern Africa and arctic regions of northern Canada, so, it's difficult to calculate the CSD in these regions. Hence, the carbonate outcrops in the above table are only those which include basic data with an area of 12.476×10^6 km^2 (the global carbonate outcrops area is about 16.698×10^6 km^2). That means the carbonate zones participated in our calculation account for 74.72% of the global carbonate zones. When we calculate the CCS, due to the large magnitude of Mexico in CCS, we separated Mexico from South America rather calculated together like our reference classification scheme (Pan et al., 2011). The data above should have followed by an uncertainty of 25.93%.

0.041 Pg C yr^{-1}) in its carbonate zones (2.156×10^6 km^2) represented 18.0% of the global CCS from 2000 to 2014. The carbonate zones in Africa (1.279×10^6 km^2) contributed a CCS of 0.077 ± 0.020 Pg C yr^{-1}, which accounts for 8.7% of the global CCS during the study period. South America (including Mexico) and Oceania represented the other 4.6% of the global CCS from 2000 to 2014, with CCS values of 0.025 ± 0.006 (2.8%) and 0.017 ± 0.004 (1.9%) Pg C yr^{-1} from 0.616×10^6 and 0.270×10^6 km^2 carbonate areas, respectively.

Within Asia, central Asia had the largest multiannual average CCS (0.110 ± 0.029 Pg C yr^{-1}) and showed an upward tendency during the study period. The Asian Russian CCS values first exhibited increasing trends and then decreasing trends, with multiannual average CCS of 0.107 ± 0.028 Pg C yr^{-1}. China had an average CCS of 0.102 ± 0.026 Pg C yr^{-1} with remarkable fluctuations in this period. The Southeast Asian CCS values (with an average of 0.070 ± 0.018 Pg C yr^{-1}) showed fluctuation tendencies that first decrease and then increase. In contrast, Japan and Korea showed steady CCS during the study period, with an average CCS of 0.005 ± 0.001 Pg C yr^{-1}. For the two regions of North America and Canada, the CCS values first showed increasing trends and then decreasing trends, with a multiannual average CCS of 0.107 ± 0.028 Pg C yr^{-1}. The CCS in the United States presented a decreasing trend, with an average of 0.080 ± 0.021 Pg C yr^{-1}. In Europe, the South European CCS showed a trend of first increasing and then decreased, with an average CCS of 0.101 ± 0.026 Pg C yr^{-1}. The CCS of European Russia presented a decreasing trend with an average value of 0.056 ± 0.015 Pg C yr^{-1}. Similarly, the North European CCS showed the same tendency as those of European Russia, with an average CCS of 0.005 ± 0.001 Pg C yr^{-1}. The African CCS exhibited a slight decreasing trend during this period, with the biggest CCS occurring in 2000. The South American CCS showed a decreasing trend, with an average CCS of 0.033 ± 0.009 Pg C yr^{-1}. Mexico, though it has a smaller carbonate zone area (0.233×10^6 km^2) than that of Oceania, showed a multiannual average CCS of 0.026 ± 0.007 Pg C yr^{-1}, which is 1.6 times that of Oceania.

Here, this study presented the national measurement of 142 countries or regions for CCS not only in magnitude but also in the spatial distribution of each nation (Figs. 5 and 6, Table 5). The estimates of the CCS for the countries with carbonate rock outcrops showed that Russia had the largest CCS in the world, with a value of 0.163 Pg C yr^{-1}, followed by Canada, presenting a CCS of 0.107 Pg C yr^{-1}. China ranked third, showing a CCS of 0.102 Pg C yr^{-1}, and the USA exhibited a CCS of 0.08 Pg C yr^{-1}, making it the fourth largest. These four countries' total CCS (0.452 Pg C yr^{-1}) accounts for more than half (50.56%) of the world's total CCS (0.894 Pg C yr^{-1}).

4. Discussion

4.1. Comparisons with studies from the same field

The multiannual averages of our estimated CCS (0.894 ± 0.232 Pg C yr^{-1}) are within the scope of the research results from this (0.15 to 1.50 Pg C yr^{-1}), showing similar results to several studies (Table 6). Notably, although these studies have made outstanding contributions to the determination of CCS values, these studies generally used limited point data from field stations, resulting in obviously different results (ranging from 0.15 to 1.50 Pg C yr^{-1}) and high uncertainties. Furthermore, these limited point data also lead to poor spatiotemporal representativeness and expandability of the estimates. Therefore, combining global long-term high-spatiotemporal-resolution ecological, meteorological and hydrological remote sensing data with long-term field monitoring data based on a global thermodynamic dissolution model that fully considers the actual hydrological, meteorological and geochemical conditions of specific regions can effectively make up for the lacking of the previous estimates, which means that the new estimates of the CCS and CCSF have higher spatiotemporal representativeness and expandability because the results of each pixel are calculated separately based on the actual hydrological and meteorological conditions of specific time series.

Table 5
Global annual total and multi-annual average CCS (Pg C yr^{-1}) of countries from 2000 to 2014.

Countries	Annual total CCS and multi-annual average CCS (Pg C yr^{-1}) of countries from 2000 to 2014															
	2000	2001	2002	2003	2004	2005	2006	2007	2008	2009	2010	2011	2012	2013	2014	Mean
Russia	0.181	0.156	0.148	0.171	0.147	0.152	0.192	0.176	0.170	0.175	0.176	0.160	0.160	0.118	0.157	0.163
Canada	0.116	0.103	0.088	0.096	0.096	0.129	0.111	0.120	0.122	0.106	0.105	0.101	0.105	0.098	0.108	0.107
China	0.106	0.100	0.113	0.095	0.088	0.100	0.088	0.102	0.119	0.087	0.113	0.092	0.105	0.101	0.115	0.102
United States	0.089	0.070	0.081	0.091	0.098	0.066	0.073	0.068	0.086	0.092	0.078	0.089	0.067	0.079	0.076	0.080
Indonesia	0.037	0.031	0.018	0.027	0.022	0.032	0.025	0.036	0.047	0.030	0.049	0.040	0.040	0.045	0.026	0.034
India	0.022	0.029	0.022	0.036	0.025	0.035	0.032	0.035	0.032	0.026	0.038	0.039	0.036	0.046	0.032	0.032
Mexico	0.021	0.022	0.028	0.028	0.022	0.026	0.022	0.025	0.032	0.019	0.036	0.027	0.022	0.036	0.029	0.026
Kazakhstan	0.032	0.025	0.022	0.035	0.026	0.018	0.028	0.025	0.022	0.027	0.023	0.030	0.025	0.023	0.015	0.025
Brazil	0.028	0.021	0.019	0.015	0.023	0.023	0.025	0.015	0.020	0.021	0.019	0.020	0.012	0.017	0.012	0.019
Ukraine	0.016	0.017	0.014	0.013	0.016	0.015	0.015	0.015	0.017	0.018	0.022	0.010	0.017	0.010	0.014	0.015
Australia	0.024	0.015	0.010	0.013	0.013	0.014	0.009	0.013	0.015	0.014	0.016	0.022	0.012	0.015	0.014	0.015
Turkey	0.017	0.025	0.014	0.018	0.012	0.011	0.013	0.013	0.008	0.018	0.014	0.013	0.017	0.007	0.015	0.014
France	0.017	0.012	0.014	0.009	0.009	0.009	0.014	0.013	0.015	0.013	0.015	0.013	0.019	0.013	0.014	0.013
Nigeria	0.026	0.011	0.014	0.012	0.010	0.011	0.015	0.019	0.008	0.008	0.011	0.008	0.010	0.007	0.004	0.012
Papua New Guinea	0.011	0.008	0.010	0.011	0.010	0.013	0.009	0.010	0.009	0.008	0.009	0.009	0.009	0.010	0.007	0.010
Belarus	0.010	0.009	0.008	0.008	0.009	0.008	0.008	0.008	0.007	0.014	0.011	0.006	0.010	0.006	0.006	0.009
Philippines	0.010	0.008	0.006	0.007	0.006	0.008	0.006	0.007	0.012	0.010	0.007	0.013	0.009	0.009	0.007	0.008
Congo	0.010	0.005	0.011	0.011	0.006	0.004	0.005	0.009	0.008	0.009	0.005	0.010	0.009	0.007	0.006	0.008
South Africa	0.013	0.010	0.006	0.005	0.007	0.006	0.010	0.008	0.007	0.006	0.006	0.007	0.008	0.007	0.006	0.007
Iran	0.005	0.005	0.005	0.006	0.007	0.006	0.007	0.009	0.004	0.009	0.005	0.009	0.009	0.006	0.007	0.007
Gabon	0.006	0.006	0.005	0.004	0.005	0.004	0.005	0.009	0.001	0.006	0.011	0.007	0.010	0.007	0.011	0.007
United Kingdom	0.009	0.004	0.007	0.004	0.005	0.004	0.006	0.005	0.007	0.007	0.005	0.006	0.010	0.004	0.005	0.006
Italy	0.007	0.003	0.007	0.005	0.005	0.006	0.003	0.004	0.007	0.006	0.008	0.004	0.007	0.005	0.008	0.006
Spain	0.006	0.003	0.005	0.005	0.004	0.004	0.004	0.004	0.007	0.005	0.006	0.003	0.005	0.004	0.003	0.004
Ireland	0.006	0.003	0.005	0.003	0.003	0.003	0.005	0.004	0.005	0.006	0.004	0.005	0.005	0.002	0.004	0.004
Laos	0.007	0.008	0.003	0.002	0.001	0.004	0.002	0.002	0.002	0.002	0.003	0.005	0.003	0.004	0.003	0.003
Other countries or regions	0.148	0.136	0.150	0.143	0.137	0.153	0.155	0.163	0.160	0.163	0.193	0.173	0.170	0.157	0.163	0.158
Global	0.979	0.849	0.833	0.872	0.813	0.866	0.887	0.916	0.949	0.904	0.989	0.923	0.914	0.842	0.870	0.894

The above table only presents those countries with relatively significant CCS. Other countries represent a set of those countries with small CCS. All CCS above should have followed by an uncertainty of 25.93%. Hence, the global multi-annual average CCS is 0.894 ± 0.232 Pg C yr^{-1}. The CCS distributions of other 116 countries or regions from 2000 to 2014 are showed in Fig. 6.

Table 6
Estimates of global CCS from different studies.

Sources	Date	Estimate method	Details	Magnitude
Yuan (1997)	1997	Estimate from the concentration of bicarbonate in the world's typical watershed drainage.	Based on case studies of 13 monitoring sites in China and then extrapolated from similar global data set.	0.61
Gaillardet et al. (1999)	1999	Compiled data from the world's 60 largest watersheds.	Calculated CCS of the world's 60 largest watersheds. In addition, carbon sinks of silicate weathering are also calculated.	0.15
Liu and Zhao (2000)	2000	Estimate using the concentrations of bicarbonate in watershed drainage.	A variety of methods are used to calculate the CCS of China based on an area ratio and the extrapolated estimated dissolution rates of the global carbonate zones.	0.42
		Carbonate rock table corrosion model.		0.41
		Diffusion boundary layer model.		1.50
Gombert (2002)	2002	Thermodynamic equilibrium estimates based on meteorological station data.	Used multiple meteorological stations data and a model that fully considers the actual hydrological and hydrochemical conditions of specific carbonate regions.	0.3
Liu et al. (2010)	2010	Estimate using the concentration of bicarbonate in the world's typical watershed drainage.	Sixteen meteorological stations datasets were used to estimate the global sinks from the dissolution mechanism.	0.82
Martin (2017)	2016	Coupled global mapping of lithology with the GEM-CO_2 model as well as watershed composition.	Using global mapping of lithology (Suchet et al., 2003), not only of the estimated the CCS of carbonate zones but also of the shale.	0.80
This paper		Thermodynamic equilibrium estimates based on global high spatial resolution hydrological, meteorological and geochemical data, coupled with a machine learning algorithm.	Used global high spatial resolution hydrological and meteorological data (raster data, not point data) and long-term field monitoring data based on a model that fully considers the actual hydrological and hydrochemical conditions of specific carbonate regions. Separately calculated CCS of each pixel with a resolution of 0.05°.	0.89

4.2. Comparison with the net forest sink

Our estimated CCS amounts to 74.50% of the global net forest sink (NFS) (1.20 ± 0.85 Pg C yr^{-1}), clearly demonstrating that the used to be ignored carbonate carbon sink has huge contribution to the global carbon budget and the CCS cannot be removed from the global carbon cycle system due to its significant magnitude. Notably, there are considerable differences in the magnitudes of the NFSs and the corresponding area's CCS in the different regions of the world (Fig. 7, Table 7). For example, the Canadian CCS is much greater than its NFS because the biomass C sink of the managed forests of Canada was reduced due to the biomass loss from intensified wildfires and insect outbreaks (Kurz et al., 2008). As a result of the negative NFSs in South Asia and South America (including Mexico), the CCS in these regions are greater than the corresponding NFSs. Notably, the Central Asian carbonate zones are larger than those involved in the calculation due to a lack of basic data in some regions; however, the data-lacking regions are mostly plateaus and deserts with poor climatic and hydrological environments (Mu et al., 2011), leading to low CCS values. For this reason, we hold that the estimated Central Asian CCS can basically represent the actual CCS values in this region. Similarly, although the NFS of Central Asia is unknown (Pan et al., 2011), the extreme climate characteristics and low vegetation and forest coverage (Hansen et al., 2013; Jia et al., 2015) in most of this region can only bring about disadvantageous NFS values, which makes us consider that the CCS in this region may be larger than its corresponding NFS. In contrast, the CCS in other regions are less than their corresponding NFSs. The Russian CCS amounts to 70.73% of its NFS because of the region's extremely large magnitude of carbonate zones (2.484×10^6 km^2), which is the greatest area globally. China has carbonate zones spanning 1.166×10^6 km^2, which amounts to only 46.94% that of Russia; however, the CCS of China amounts to 62.58% that of Russia because the carbonate zones in China are more concentrated in Southwest China, which enjoys plentiful rainfall and steady warm temperatures, which are conducive to the long-term sustainability of the dissolution process. For this reason, China shows a relatively large CCS, which amounts to 56.72% of its NFS. The regions of the United States and South Europe within the same latitude zones share similar CCS and NFSs due to the similar climate conditions over their carbonate zones. The African carbonate zones involved in the estimation (eliminating the deserts in northern Africa) have an area of 1.279×10^6 km^2, which accounts for 10.25% of global carbonate zones area, and its CCS amounts to 48.13% of its corresponding NFS. The rest of the regions, such as Oceania, North Europe, Japan and Korea, have relatively small CCS; the percentages to their NFSs are all >5% (amounting to 26.67%, 13.33%, and 8.33% of their corresponding NFSs). The above discussions show that the global CCS values, whether from the global scale or a regional perspective, have magnitudes that cannot be ignored and are an important component of the global terrestrial carbon sink system.

Table 7
Regional and global annual average CCS (2000–2014) in the world's carbonate zones and corresponding net forest sinks (2000–2007) (Pg C yr^{-1}) in forests.

Regions	Annual average CCS from 2000 to 2014	Annual average net forest sinks (Pan et al., 2011) from 2000 to 2007	Percentages of annual average CCS to net forest sinks
Asian Russia	0.107 ± 0.028	0.26	41.15%
European Russia	0.056 ± 0.015	0.20	28.00%
Central Asia	0.110 ± 0.029	No data	/
Canada	0.107 ± 0.028	0.01	>100%
China	0.102 ± 0.026	0.18	56.67%
South Europe	0.101 ± 0.026	0.24	42.08%
United States	0.080 ± 0.021	0.24	33.33%
Africa	0.077 ± 0.020	0.16	48.13%
Southeast Asia	0.070 ± 0.018	−0.14	>100%
South America	0.033 ± 0.009	−0.09	>100%
Mexico	0.026 ± 0.007		
Oceania	0.016 ± 0.004	0.06	26.67%
Japan & Korea	0.005 ± 0.001	0.06	8.33%
North Europe	0.004 ± 0.001	0.03	13.33%
Global	0.894 ± 0.232	1.20 ± 0.85	74.50%

Here, the percentages of regional and global CCS amounted to corresponding net forest sink are also presented in the table. The classification scheme is according to Pan's research and it's also the source of net forest C sink data (Pan et al., 2011). The net forest sinks are missing in Central Asia and the net forest sink of South America includes Mexico (Pan et al., 2011), however, when we calculate the CCS, due to the large magnitude of Mexico in CCS, we separated Mexico from South America.

4.3. Contribution to the global carbon budget

It is remarkable that according to our estimates, the global CCS accounts for 46.81% of the missing carbon sink (Table 8), which further explains the importance of the CCS. In addition, our research not only confirms an important source of the terrestrial carbon sink and missing sink but also details the magnitudes, locations and variations of the global and regional CCS. Specifically, based on the global carbon budget model (Melnikov and O'Neill, 2006), the terrestrial carbon sink is equal to the carbon emissions (fossil fuel emissions and emissions from changes in land use) minus the non-terrestrial carbon sinks (oceanic

Table 8
Global carbon budget for the study period (Pg C yr^{-1}).

Sources and sinks	Magnitudes	Periods
Sources (C emissions)		
Fossil fuel emissions[a]	7.60 ± 0.40	2000–2006
Land use emissions[b]	1.14 ± 0.18	1990–2009
Total sources	8.74 ± 0.43	
Sinks (C uptake)		
Atmospheric increase[c]	4.13 ± 0.17	1998–2011
Ocean net uptake[c]	1.50 ± 0.50	1998–2011
Forest net uptake[d]	1.20 ± 0.85	2000–2007
CCS[e]	0.89 ± 0.23	2000–2014
Total sinks	7.72 ± 1.03	
Global residual	1.02 ± 1.12	

All the magnitudes in the above table are the mean values of their study periods, which make their comparisons and calculations reasonable. The total sinks are the sum of fossil fuel emissions and land use emissions. The terrestrial sink equals the carbon emissions (sources) minus the non-terrestrial carbon sinks, which is equivalent to the magnitude of 3.11 ± 0.68 Pg C yr^{-1}. The missing sink is equal to the terrestrial sinks minus the net forest uptake, which is 1.91 ± 1.09 Pg C yr^{-1}. The global residual represents the rest of the unknown sinks or the still uncertain missing sink.

[a] For fossil fuel emissions, please see Canadell's study (Canadell et al., 2007).

[b] For the mean global emissions from land use and land-cover change (LULCC), please see Houghton's research (Hartemink et al., 2008; Houghton et al., 2012).

[c] For the carbon sinks that correspond to atmospheric increases and net ocean uptake, please see Landschützer's study (Landschutzer et al., 2014).

[d] For the net forest uptake, please see Pan's study (Pan et al., 2011).

[e] The CCS is calculated for the global carbonate zones.

uptake and atmospheric concentration increases). Hence, the terrestrial carbon sink estimated here is 3.11 ± 0.68 Pg C yr^{-1}, which is in the range (1.9–4.8 Pg C yr^{-1}) of those values given in earlier studies (Watson et al., 2000; House et al., 2003; Melnikov and O'Neill, 2006; Landschutzer et al., 2014; Poulter et al., 2014). Our estimated CCS accounts for 28.75% of the terrestrial carbon sink. After subtracting the NFS from the terrestrial sink, the global carbon budget still remains unbalanced, with a sink of approximately 1.91 ± 1.09 Pg C yr^{-1} needing to be explain, which describes the missing sink (Schindler, 1999; Nilsson et al., 2003). Our estimated CCS accounts for 46.81% of this missing sink, and thus, the global CCS is an important source of the missing sink that cannot be ignored. Based on this calculation, nearly half of the missing sink and its global distribution have been identified.

5. Conclusions

In this study, our estimates suggest that the global CCS accounts for more than one-quarter of the terrestrial sink or nearly half of the global missing sink, or amounts to 74.50% of the global net forest sink which clearly demonstrate that the used to be ignored carbonate carbon sink has huge contribution to the global carbon budget. Our global high resolution distribution maps of the CCSF have solved the problem of spatial distributions of the global and national CCSF and CCS which have plagued researchers for many years. Our national measurement of 142 countries or regions showed that every nation, regardless the size, rich and poor, the strong or weak, all have carbon emission rights as well as carbon sequestration obligations, and we should incorporate CCS into the category of national carbon measurement and global carbon trading just like forest carbon sequestration due to the huge magnitude of CCS. Also, each individual, regardless poverty and wealth, has carbon emission rights as well as carbon sequestration obligations, so the CCS should be considered in the global carbon markets. Of course, it is possible to measure the spatiotemporal magnitude of rock weathered carbon sequestration according to per capita.

Our research estimated the magnitudes, spatial distributions, variations and contributions to the global carbon budget of the CCS in a higher spatiotemporal representativeness and expandability way, which, via multiple mechanisms, introduce an important sink in the terrestrial carbon sink system and the global missing sink and that can help us further reveal and support our understanding of global rock weathering carbon sequestration, terrestrial carbon sink system and global carbon cycle dynamics which make our understanding of global change more comprehensive. According to our national measurement of CCS, CCS of 142 countries across six continents were identified and that can be a significant support for the carbon emission trading in the global carbon markets which can make the global or national carbon markets and emission trading system more complete, fairer and more legitimate.

Of cause, our research also has some limitations. For data, the long-term monitoring dataset can well exhibit the real geochemical conditions of the carbonate regions which are less affected by human activities, however, there is no denying that its expansion to the global scale still has some bias in some regions strongly affected by the human activities. Therefore, in future works, we will adopt more appropriate data and methods to solve this problem. In addition, although we have done a lot of efforts to reduce the uncertainty of the estimated results such as the data selection, processing and model building, we still have some shortcomings in the determination of the uncertainty in pixel level. In the future, we will find the right way for the spatial uncertainty distribution of each pixel.

Acknowledgments

This research work was supported jointly by National Key Research Program of China (No. 2016YFC0502300 & 2016YFC0502102), Chinese Academy of Science and Technology Services Network Program (No. KFJ-STS-ZDTP-036) and International Cooperation Agency International Partnership Program (No.132852KYSB20170029, No. 2014-3), Guizhou High-Level Innovative Talent Training Program "Ten" Level Talents Program (No. 2016-5648), United Fund of Karst Science Research Center (No. U1612441), International Cooperation Research Projects of the National Natural Science Fund Committee (No. 41571130074 & 41571130042), Science and Technology Plan of Guizhou Province of China (No. 2017–2966).

References

Bai, Z.G., Dent, D., 2009. Recent land degradation and improvement in China. Ambio 38: 150–156. https://doi.org/10.1579/0044-7447-38.3.150.

Breiman, L., 1996. Bagging predictors. Mach. Learn. 24 (2):123–140. https://doi.org/10.1023/A:1018054314350 (August).

Breiman, L., 2001. Random forests. Mach. Learn. 45:5–32. https://doi.org/10.1023/A:1010933404324.

Brook, G.A., Folkoff, M.E., Box, E.O., 1983. A world model of soil carbon-dioxide. Earth Surf. Process. Landf. 8:79–88. https://doi.org/10.1002/esp.3290080108.

Canadell, J.G., Le Quere, C., Raupach, M.R., Field, C.B., Buitenhuis, E.T., Ciais, P., Conway, T.J., Gillett, N.P., Houghton, R.A., Marland, G., 2007. Contributions to accelerating atmospheric CO_2 growth from economic activity, carbon intensity, and efficiency of natural sinks. Proc. Natl. Acad. Sci. U. S. A. 104:18866–18870. https://doi.org/10.1073/pnas.0702737104.

Chen, M.Y., Shi, W., Xie, P.P., Silva, V.B.S., Kousky, V.E., Higgins, R.W., Janowiak, J.E., 2008. Assessing objective techniques for gauge-based analyses of global daily precipitation. J. Geophys. Res.-Atmos. 113. https://doi.org/10.1029/2007JD009132.

Dreybrodt, W., 1988. Processes in Karst Systems. Springer, Berlin, Heidelberg https://doi.org/10.1007/978-3-642-83352-6.

Evensen, G., 2013. Data Assimilation. Springer, Berlin, Heidelberg https://doi.org/10.1007/978-3-642-03711-5.

Fernandez-Delgado, M., Cernadas, E., Barro, S., Amorim, D., 2014. Do we need hundreds of classifiers to solve real world classification problems? J. Mach. Learn. Res. 15, 3133–3181.

Gaillardet, J., Dupre, B., Louvat, P., Allegre, C.J., 1999. Global silicate weathering and CO_2 consumption rates deduced from the chemistry of large rivers. Chem. Geol. 159: 3–30. https://doi.org/10.1016/S0009-2541(99)00031-5.

Gombert, P., 2002. Role of karstic dissolution in global carbon cycle. Glob. Planet. Chang. 33:177–184. https://doi.org/10.1016/S0921-8181(02)00069-3.

Guo, L., Ma, Y., Cukic, B., Singh, H., 2004. Robust prediction of fault-proneness by random forests. 15th International Symposium on Software Reliability Engineering, Proceedings, pp. 417–428.

Hansen, M.C., Potapov, P.V., Moore, R., Hancher, M., Turubanova, S.A., Tyukavina, A., Thau, D., Stehman, S.V., Goetz, S.J., Loveland, T.R., Kommareddy, A., Egorov, A., Chini, L., Justice, C.O., Townshend, J.R.G., 2013. High-resolution global maps of 21st-century forest cover change. Science 342:850–853. https://doi.org/10.1126/science.1244693.

Hartemink, A.E., Veldkamp, T., Bai, Z.G., 2008. Land cover change and soil fertility decline in tropical regions. Turk. J. Agric. For. 32, 195–213.

Houghton, R.A., Werf, G.R.V.D., Defries, R.S., Hansen, M.C., House, J.I., Quéré, C.L., Pongratz, J., Ramankutty, N., 2012. Chapter G2 carbon emissions from land use and land-cover change. Biogeosciences 9:5125–5142. https://doi.org/10.5194/bgd-9-835-2012.

House, J.I., Prentice, I.C., Ramankutty, N., Houghton, R.A., Heimann, M., 2003. Reconciling apparent inconsistencies in estimates of terrestrial CO_2 sources and sinks. Tellus B 55:345–363. https://doi.org/10.1034/j.1600-0889.2003.00037.x.

Jia, K., Liang, S.L., Liu, S.H., Li, Y.W., Xiao, Z.Q., Yao, Y.J., Jiang, B., Zhao, X., Wang, X.X., Xu, S., Cui, J., 2015. Global land surface fractional vegetation cover estimation using general regression neural networks from MODIS surface reflectance. IEEE Trans. Geosci. Remote Sens. 53:4787–4796. https://doi.org/10.1109/TGRS.2015.2409563.

Kurz, W.A., Stinson, G., Rampley, G.J., Dymond, C.C., Neilson, E.T., 2008. Risk of natural disturbances makes future contribution of Canada's forests to the global carbon cycle highly uncerain. Proc. Natl. Acad. Sci. U. S. A. 105:1551–1555. https://doi.org/10.1073/pnas.0708133105.

Landschutzer, P., Gruber, N., Bakker, D.C.E., Schuster, U., 2014. Recent variability of the global ocean carbon sink. Glob. Biogeochem. Cycles 28:927–949. https://doi.org/10.1002/2014GB004853.

Li, B.G., Gasser, T., Ciais, P., Piao, S.L., Tao, S., Balkanski, Y., Hauglustaine, D., Boisier, J.P., Chen, Z., Huang, M.T., Li, L.Z., Li, Y., Liu, H.Y., Liu, J.F., Peng, S.S., Shen, Z.H., Sun, Z.Z., Wang, R., Wang, T., Yin, G.D., Yin, Y., Zeng, H., Zeng, Z.Z., Zhou, F., 2016a. The contribution of China's emissions to global climate forcing. Nature 531 (7594):357. https://doi.org/10.1038/nature17165.

Li, Y., Bai, X., Zhou, Y., Qin, L., Tian, X., Tian, Y., Li, P., 2016b. Spatial–temporal evolution of soil erosion in a typical mountainous Karst Basin in SW China, based on GIS and RUSLE. Arab. J. Sci. Eng. 41:209–221. https://doi.org/10.1007/s13369-015-1742-6.

Liu, Z., Dreybrodt, W., 2015. Significance of the carbon sink produced by H_2O-carbonate-CO_2-aquatic phototroph interaction on land. Sci. Bull. 60:182–191. https://doi.org/10.1007/s11434-014-0682-y.

Liu, Z., Zhao, J., 2000. Contribution of carbonate rock weathering to the atmospheric CO_2 sink. Environ. Geol. 39:1053–1058. https://doi.org/10.1007/s002549900072.

Liu, Z.H., Dreybrodt, W., Wang, H.J., 2010. A new direction in effective accounting for the atmospheric CO_2 budget: considering the combined action of carbonate dissolution, the global water cycle and photosynthetic uptake of DIC by aquatic organisms. Earth-Sci. Rev. 99:162–172. https://doi.org/10.1016/j.earscirev.2010.03.001.

Liu, Z.H., Dreybrodt, W., Liu, H., 2011. Atmospheric CO_2 sink: silicate weathering or carbonate weathering? Appl. Geochem. 26:S292–S294. https://doi.org/10.1016/j.apgeochem.2011.03.085.

Martin, J.B., 2017. Carbonate minerals in the global carbon cycle. Chem. Geol. 449:58–72. https://doi.org/10.1016/j.chemgeo.2016.11.029.

Martin, J.B., Brown, A., Ezell, J., 2013. Do carbonate karst terrains affect the global carbon cycle? Acta Carsologica 42:187–196. https://doi.org/10.3986/ac.v42i2-3.660.

Melnikov, N.B., O'Neill, B.C., 2006. Learning about the carbon cycle from global budget data. Geophys. Res. Lett. 33:356–360. https://doi.org/10.1029/2005GL023935.

Mu, Q.Z., Zhao, M.S., Running, S.W., 2011. Improvements to a MODIS global terrestrial evapotranspiration algorithm. Remote Sens. Environ. 115:1781–1800. https://doi.org/10.1016/j.rse.2011.02.019.

Nilsson, S., Jonas, M., Stolbovoi, V., Shvidenko, A., Obersteiner, M., McCallum, I., 2003. The missing "missing sink". For. Chron. 79:1071–1074. https://doi.org/10.5558/tfc791071-6.

Pan, Y.D., Birdsey, R.A., Fang, J.Y., Houghton, R., Kauppi, P.E., Kurz, W.A., Phillips, O.L., Shvidenko, A., Lewis, S.L., Canadell, J.G., Ciais, P., Jackson, R.B., Pacala, S.W., McGuire, A.D., Piao, S.L., Rautiainen, A., Sitch, S., Hayes, D., 2011. A large and persistent carbon sink in the world's forests. Science 333:988–993. https://doi.org/10.1126/science.1201609.

Plummer, L.N., Busenberg, E., 1982. The solubilities of calcite, aragonite and vaterite in CO_2-H_2O solutions between 0 and 90 °C, and an evaluation of the aqueous model for the system $CaCO_3$-CO_2-H_2O. Geochim. Cosmochim. Acta 46:1011–1040. https://doi.org/10.1016/0016-7037(82)90056-4.

Pokrovsky, O.S., Golubev, S.V., Schott, J., 2005. Dissolution kinetics of calcite, dolomite and magnesite at 25 degrees C and 0 to 50 atm pCO_2. Chem. Geol. 217:239–255. https://doi.org/10.1016/j.chemgeo.2004.12.012.

Poulter, B., Frank, D., Ciais, P., Myneni, R.B., Andela, N., Bi, J., Broquet, G., Canadell, J.G., Chevallier, F., Liu, Y.Y., Running, S.W., Sitch, S., van der Werf, G.R., 2014. Contribution of semi-arid ecosystems to interannual variability of the global carbon cycle. Nature 509 (7502):600. https://doi.org/10.1038/nature13376.

Raupach, M.R., 2011. CARBON CYCLE Pinning down the land carbon sink. Nat. Clim. Chang. 1:148–149. https://doi.org/10.1038/nclimate1123.

Reshef, D.N., Reshef, Y.A., Finucane, H.K., Grossman, S.R., McVean, G., Turnbaugh, P.J., Lander, E.S., Mitzenmacher, M., Sabeti, P.C., 2011. Detecting novel associations in large data sets. Science 334:1518–1524. https://doi.org/10.1126/science.1205438.

Rodriguez-Galiano, V., Mendes, M.P., Garcia-Soldado, M.J., Chica-Olmo, M., Ribeiro, L., 2014. Predictive modeling of groundwater nitrate pollution using Random Forest and multisource variables related to intrinsic and specific vulnerability: a case study in an agricultural setting (Southern Spain). Sci. Total Environ. 476:189–206. https://doi.org/10.1016/j.scitotenv.2014.01.001.

Rubel, F., Kottek, M., 2010. Observed and projected climate shifts 1901–2100 depicted by world maps of the Koppen-Geiger climate classification. Meteorol. Z. 19:135–141. https://doi.org/10.1127/0941-2948/2010/0430.

Schindler, D.W., 1999. Carbon cycling - the mysterious missing sink. Nature 398 (6723): 105–107. https://doi.org/10.1038/18111.

Shen, T.M., Li, W., Pan, W.Z., Lin, S.Y., Zhu, M., Yu, L.J., 2017. Role of bacterial carbonic anhydrase during CO_2 capture in the CO_2-H_2O-carbonate system. Biochem. Eng. J. 123:66–74. https://doi.org/10.1016/j.bej.2017.04.003.

Suchet, P.A., Probst, J.L., Ludwig, W., 2003. Worldwide distribution of continental rock lithology: implications for the atmospheric/soil CO_2 uptake by continental weathering and alkalinity river transport to the oceans. Glob. Biogeochem. Cycles 17. https://doi.org/10.1029/2002GB001891.

Tian, Y.C., Wang, S.J., Bai, X.Y., Luo, G.J., Xu, Y., 2016. Trade-offs among ecosystem services in a typical Karst watershed, SW China. Sci. Total Environ. 566:1297–1308. https://doi.org/10.1016/j.scitotenv.2016.05.190.

Van Oost, K., Quine, T.A., Govers, G., De Gryze, S., Six, J., Harden, J.W., Ritchie, J.C., McCarty, G.W., Heckrath, G., Kosmas, C., Giraldez, J.V., da Silva, J.R.M., Merckx, R., 2007. The impact of agricultural soil erosion on the global carbon cycle. Science 318:626–629. https://doi.org/10.1126/science.1145724.

Verikas, A., Gelzinis, A., Bacauskiene, M., 2011. Mining data with random forests: a survey and results of new tests. Pattern Recogn. 44:330–349. https://doi.org/10.1016/j.patcog.2010.08.011.

Wang, S.J., Li, R.L., Sun, C.X., Zhang, D.F., Li, F.Q., Zhou, D.Q., Xiong, K.N., Zhou, Z.F., 2004. How types of carbonate rock assemblages constrain the distribution of karst rocky desertified land in Guizhou Province, PR China: phenomena and mechanisms. Land Degrad. Dev. 15:123–131. https://doi.org/10.1002/ldr.591.

Watson, R.T., Noble, I.R., Bolin, B., Ravindranath, N.H., Verardo, D.J., Dokken, D.J., Watson, R.T., Noble, I.R., Bolin, B., Ravindranath, N.H., 2000. Land use, land-use change and forestry: a special report of the Intergovernmental Panel on Climate Change. https://www.ipcc.ch/pdf/special-reports/spm/srl-en.pdf.

Yuan, D., 1997. The carbon cycle in karst. Z. Geomorphol. 108, 91–102.

Zeng, S.B., Jiang, Y.J., Liu, Z.H., 2016. Assessment of climate impacts on the karst-related carbon sink in SW China using MPD and GIS. Glob. Planet. Chang. 144:171–181. https://doi.org/10.1016/j.gloplacha.2016.07.015.

Zeng, C., Wang, S.J., Bai, X.Y., Li, Y.B., Tian, Y.C., Li, Y., Wu, L.H., Luo, G.J., 2017. Soil erosion evolution and spatial correlation analysis in a typical karst geomorphology using RUSLE with GIS. Solid Earth 8:721–736. https://doi.org/10.5194/se-8-721-2017.

Zhang, H., Wu, P.B., Yin, A.J., Yang, X.H., Zhang, M., Gao, C., 2017. Prediction of soil organic carbon in an intensively managed reclamation zone of eastern China: a comparison of multiple linear regressions and the random forest model. Sci. Total Environ. 592: 704–713. https://doi.org/10.1016/j.scitotenv.2017.02.146.